Chemical Science

ROYAL SOCIETY OF CHEMISTRY

EDGE ARTICLE

View Article Online
View Journal | View Issue

Cite this: *Chem. Sci.*, 2025, **16**, 3655

All publication charges for this article have been paid for by the Royal Society of Chemistry

A mesityl-functionalized double-boron–nitrogen–oxygen-embedded multi-resonance framework achieves anti-quenching narrowband deep-blue electroluminescence with EQE over 30% and CIE$_y$ of 0.046†

Zhuixing Xue, Zhengqi Xiao, Yang Zou, Zhanxiang Chen, Jiahui Liu, Zhongyan Huang * and Chuluo Yang *

Developing highly efficient deep-blue multi-resonance thermal activated delayed fluorescence (MR-TADF) materials for ultra-high-definition organic light-emitting diodes (OLEDs) displays that meet the stringent BT.2020 standard remains a significant challenge. In this study, we present a strategy to achieve high-performance deep-blue MR-TADF emitters by integrating a large π-conjugated double-boron-embedded MR skeleton with strategically positioned peripheral steric hindrance groups. The developed molecule, **DMBNO**, exhibits a narrow full-width at half maximum (FWHM) of 19 nm, with a deep-blue emission peak at 444 nm in diluted toluene solutions. Additionally, it achieves high photoluminescence quantum yield (PLQY) and a horizontal ratio of emitting dipole orientation ($\theta_{\parallel}$) exceeding 90% in doped films. Notably, **DMBNO** demonstrates anti-quenching properties and effectively suppresses spectrum broadening. Consequently, OLEDs based on **DMBNO** achieve a high maximum external quantum efficiency (EQE$_{max}$) of 32.3%, with an impressive Commission Internationale de l'Eclairage (CIE) *y*-coordinate of 0.046, fully satisfying the BT.2020 blue gamut at a high doping concentration of 10 wt%. These findings offer valuable insights into molecular design tactics for deep-blue MR-TADF emitters featuring high efficiency, ultra-pure color, and anti-quenching characteristics.

Received 6th November 2024
Accepted 7th January 2025

DOI: 10.1039/d4sc07503j

rsc.li/chemical-science

Introduction

The development of deep-blue organic light-emitting diodes (OLEDs) with high efficiency and narrowband emission is crucial for enabling efficient ultrahigh-definition (UHD) displays.[1] However, creating emitters that can concurrently achieve 100% exciton utilization and ultrapure-blue emission to fully meet the BT.2020 blue gamut in electroluminescence (EL) remains a pivotal challenge.[2,3] To fulfill the BT.2020 blue gamut, emitters must not only exhibit appropriate blue-region emission peaks but also possess a narrow bandwidth.[4] Unfortunately, conventional blue organic emitters typically suffer from broad bandwidths, which arise from intermolecular charge transfer (CT) excited states.[5–7]

To address this challenge, multi-resonance organic thermally activated delayed fluorescence (MR-TADF) emitters have emerged as a promising solution. In 2016, Hatakeyama *et al.*[8] introduced the first MR-TADF molecule, DABNA-1, based on a rigid boron/nitrogen embedded polycyclic aromatic hydrocarbon (PAH) framework. This molecule achieved an EL peak of 459 nm with a narrow full-width at half maximum (FWHM) of 28 nm, corresponding to Commission Internationale de l'Éclairage (CIE) coordinates of (0.13, 0.09), and a maximum external quantum efficiency (EQE$_{max}$) of 13.5%. Since then, significant efforts have been dedicated to this field, resulting in the rapid development of numerous highly efficient blue MR-TADF emitters with narrowband emission through diverse molecular design tactics.[9–22] Among these, π-extension of the MR framework with multi-boron fusion has proven particularly effective in realizing deep-blue emission with ultra-narrow FWHMs and high EQEs.[23–31] For instance, our group recently reported a four-boron-embedded deep-blue emitter, DPA-B4, demonstrating ultra-high EQE of 39.2% and CIE coordinates of (0.141, 0.050).[32] However, extending the conjugated structure often increases molecular planarity, which leads to aggregation-induced quenching (ACQ) at high doping concentration due to π–π stacking, as well as redshifts of the emission spectrum.[33,34] Thus, resolving the issues arising from π–π stacking in these

Shenzhen Key Laboratory of New Information Display and Storage Materials, College of Materials Science and Engineering, Shenzhen University, Shenzhen, 518060, P. R. China. E-mail: zyhuang@szu.edu.cn; clyang@szu.edu.cn

† Electronic supplementary information (ESI) available. CCDC 2385105 and 2385106. For ESI and crystallographic data in CIF or other electronic format see DOI: https://doi.org/10.1039/d4sc07503j

large planar molecules is essential for the development of high-performance deep-blue MR-TADF molecules.

To suppress the ACQ effect and spectral broadening in MR-TADF molecules, some tactics have been investigated.[35–40] For example, in 2021, our group reported a strategy involving the incorporation of carbazole groups on opposite sides of the planar MR core, significantly mitigating intermolecular π–π stacking. This strategy enhanced EL performance, achieving EQEs exceeding 30% and maintained nearly identical narrowband EL spectra across doping concentrations ranging from 1 wt% to 30 wt% (Fig. 1).[35] Subsequently, Jiang *et al.*[36] introduced a spiro strategy to construct shield-like molecule with anti-quenching characteristics (Fig. 1). While these emitters demonstrated high efficiency and quenching resistance, their EL peaks fell in the bluish-green region. Recently, Xu *et al.*[41] employed an ambipolar self-host functionalized tactic to develop a blue MR-TADF emitter, **tCBNDADPO**, which achieved EQEs of up to 30.8% with CIE coordinates of (0.14, 0.22) at a doping concentration of 30 wt%. Additionally, Kim *et al.*[42] developed a deep-blue MR-TADF emitter, ***p*BP-DABNA-Me**, by introducing biphenyls and *N*-biphenyl-*N*-*ortho*-dimethylphenylamine substituents to create dense local triplet states and suppress intramolecular aggregation. The resulting devices demonstrated EQE over 20%, with consistent EL peaks at 464 nm, small FWHMs of 23 nm, and CIE coordinates of (0.132, 0.092) across doping concentrations from 5% to 20 wt% (Fig. 1). Nevertheless, these emitters still failed to meet the BT.2020 blue standard, which requires CIE coordinates of (0.131, 0.046).

Given the above discussion, developing MR-TADF emitters that achieve concurrently deep-blue emission with CIE_y of 0.046 and anti-quenching properties remains a formidable challenge. In this study, we propose a simple yet effective molecular design strategy to achieve superior deep-blue emitters with high color purity, high efficiency, and quenching resistance (Fig. 1). Distinct from the previously reported anti-quenching MR-TADF emitters, we chose a double-boron–nitrogen–oxygen (B–N–O) embedded framework as the MR skeleton, which offers deep-blue emission, high photoluminescence quantum yield (PLQY), and high horizontal ratios of emitting dipole orientation ($\theta_{\parallel}$). Subsequently, we decorated the planar MR framework peripherally with multi-mesityl groups. However, **DBNO**, which only possesses two mesityl groups, exhibits similar performance as its analogue DOBN,[43] without significant aggregation inhibition. Interestingly, the addition of two additional mesityl units results in only a negligible redshift in the emission while maintaining excellent color purity. Moreover, this decoration effectively inhibits π–π stacking between the MR planes. Notably, OLEDs based on the proof-of-concept emitter, **DMBNO**, demonstrated high EQEs ranging from 30.0% to 32.3% within the doping concentration range of 5–15 wt%. Critically, at a doping concentration of 10 wt%, the OLED exhibited deep-blue emission peaking at 449 nm, an excellent EQE of 32.3%, and a CIE_y of 0.046, fully satisfying the BT.2020

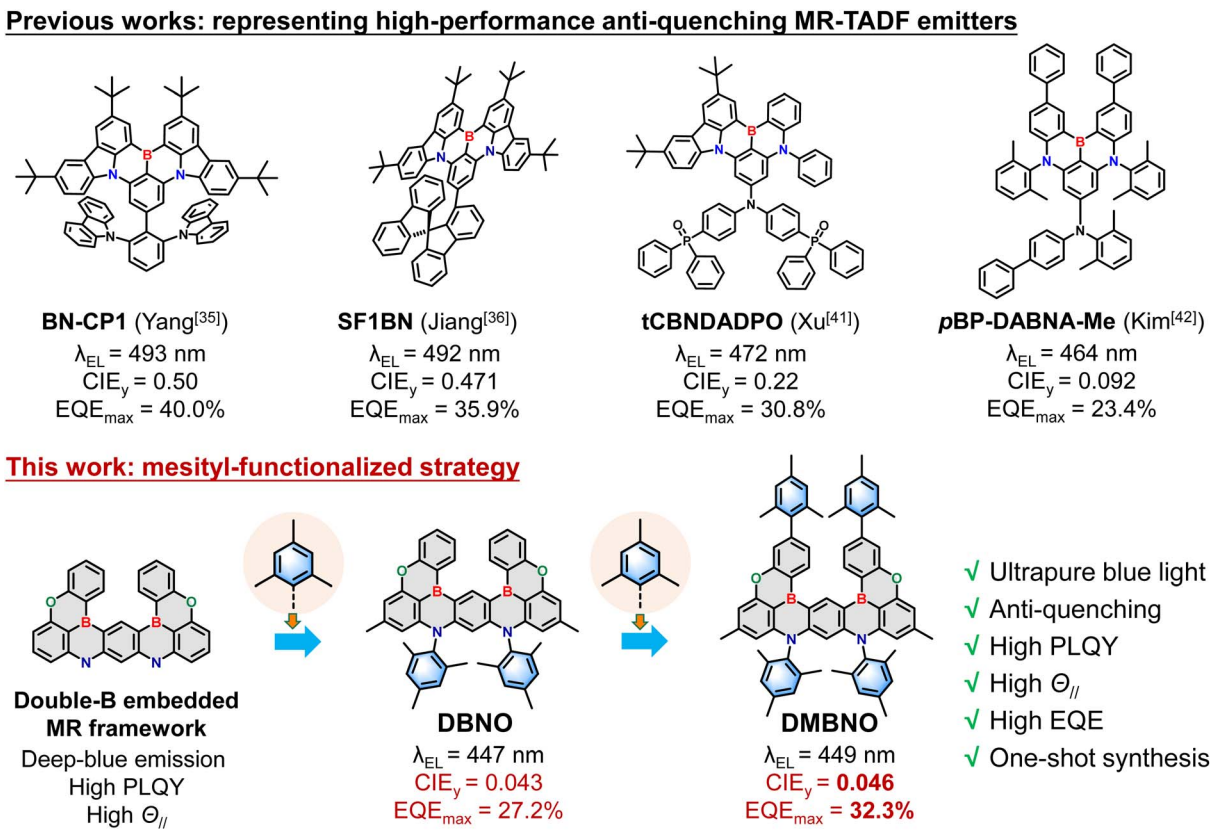

Fig. 1 Chemical structure and molecular design strategy of anti-quenching MR-TADF emitters.

blue gamut. This result places **DMBNO** among the most promising pure-organic emitters with deep-blue emission.

Results and discussion

Synthesis and characterization

The chemical structure of the designed molecules, **DBNO** and **DMBNO**, are illustrated in Fig. 1. These compounds were successfully synthesized *via* one-shot regioselective borylation reaction from key intermediates 4 or 5, as described in our previous report (Fig. 2a).[44] Detailed synthetic procedures can be found in the ESI.† All synthesized compounds were thoroughly characterized using nuclear magnetic resonance (NMR) spectroscopy, and the final compounds were further verified by high-resolution mass spectrometry (HRMS) and single crystal X-ray diffraction. Cyclic voltammetry (CV) measurements revealed the highest occupied molecular orbital (HOMO) energy levels of **DBNO** and **DMBNO** to be −5.35 eV and −5.36 eV, respectively (Fig. S18†). Based on the optical gaps of 2.81 eV and 2.78 eV, the lowest unoccupied molecular orbital (LUMO) energy levels were calculated as −2.54 eV for **DBNO** and −2.58 eV for **DMBNO**. Thermogravimetric analysis (TGA) confirmed the thermal stability of **DBNO** and **DMBNO**, with decomposition temperature (T_d, corresponding to 5% mass loss) of 400 °C and 410 °C, respectively (Fig. S19†). The excellent thermal stability is advantageous for the vacuum-deposited process in OLED fabrication.

The crystal structures of these molecules reveal a large planar of the B–N–O MR core, which ensures an optimal planar framework that is key for achieving a high $\theta_{\parallel}$ (Fig. 2b). With two mesityl groups attached to the nitrogen atoms, **DBNO** exhibits a nearly perpendicular conformation (88.5°) between the MR framework and the peripheral mesityl unit, which can distort the molecule skeleton and suppress intermolecular interactions. In comparison to **DBNO**, **DMBNO** contains additional two mesityl groups at the *para*-position of the boron atoms with a large torsion angle of 78.5°, which significantly increases the intermolecular stacking distance, thereby effectively suppressing the π–π stacking between molecules in the solid states. As a result, the configuration of **DMBNO** is thus beneficial for solid-state emission.

Theoretical calculations

To gain deeper insight into the electronic configurations of the designed emitters, computational simulations were conducted based on the density functional theory (DFT) and time-dependent DFT (TD-DFT) calculations. As shown in Fig. 3, both emitters exhibit typical MR features with localized frontier molecular orbitals (FMOs) distribution centered on the MR core. Notably, the absence of FMOs distributions on the peripheral mesityl groups suggests that these decorating units will have minimal influence on the luminescent behavior of the emitters. This is further supported by the similar highest occupied molecular orbital (HOMO) and lowest unoccupied molecular orbital (LUMO) energy levels of **DBNO** (−5.06 and −1.50 eV) and **DMBNO** (−5.06 and −1.51 eV), indicating similar emission characteristics for both emitters. Both **DBNO** and **DMBNO** exhibit high and almost identical lowest singlet energy level (S_1) with values of 3.07 eV and 3.05 eV, respectively, indicating their potential to produce deep-blue emission. Furthermore, the predicted high oscillation strength (*f*) values (0.3174 for **DBNO** and 0.3525 for **DMBNO**) of the emitters signify their high radiative decay rates, which contribute high PLQY. Additionally, both emitters exhibit small reorganization energies (Fig. 3b and d), indicating that structural variations between the

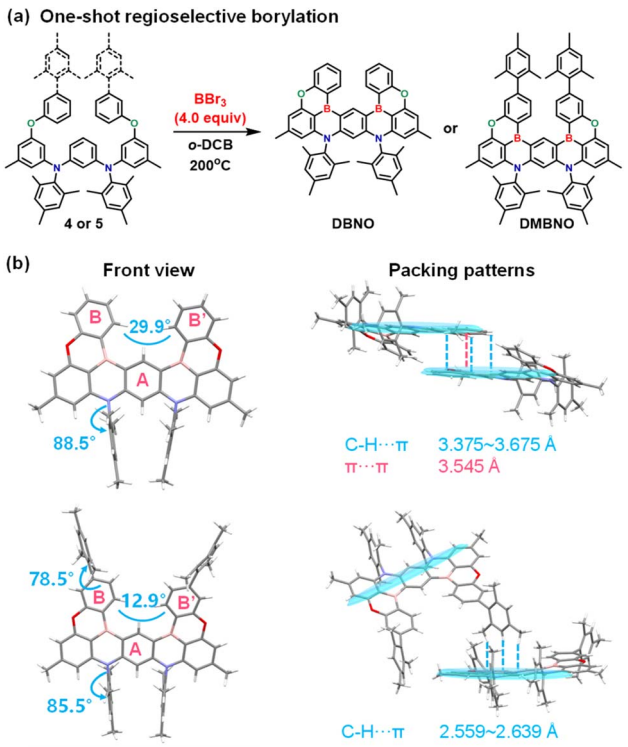

Fig. 2 (a) Synthetic route of **DBNO** and **DMBNO**. (b) Single-crystal structure of **DBNO** (CCDC: 2385105) and **DMBNO** (CCDC: 2385106).

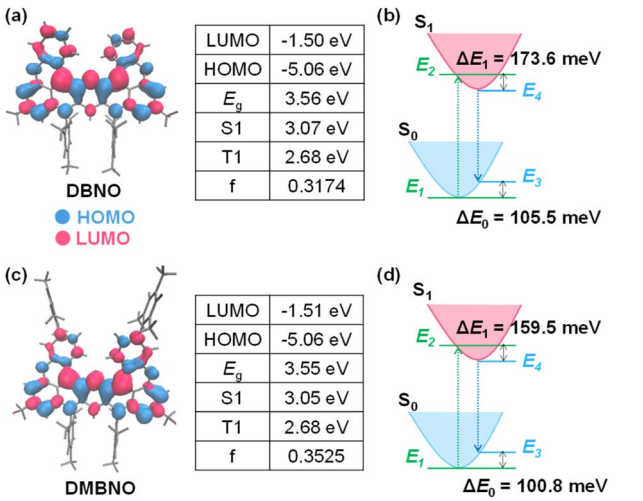

Fig. 3 The frontier molecular orbital distributions, energy levels, and reorganization energies of **DBNO** (a and b) and **DMBNO** (c and d).

ground state (S_0) and S_1 are effectively minimized. Interestingly, the total reorganization energy of **DMBNO** (260.3 meV) is slightly smaller than that of **DBNO** (279.1 meV), suggesting the **DMBNO** may exhibit a narrower FWHM in its emission spectrum.

Photophysical properties

To investigate the photophysical properties of the emitters, we recorded ultraviolet-visible (UV-vis) absorption, steady-state fluorescence (Fl, at 300 K), and low-temperature (77 K) Fl and phosphorescence (Phos) spectra of **DBNO** and **DMBNO** in diluted toluene solutions (1×10^{-5} M). As shown in Fig. 4a, both emitters exhibit distinct absorption peaks below 360 nm, attributed to π–π* and n–π* transitions of the molecules. Notably, long-wavelength absorption peaks around 430 nm originate from intramolecular charge transfer (ICT) within the emitters. **DMBNO** displays a slight 3 nm redshift in ICT absorption compared to **DBNO**, suggesting a minor redshift in its emission. Both emitters exhibit narrowband deep-blue emission, with peak/FWHM values of 443/21 nm for **DBNO** and 444/19 nm for **DMBNO**, resulting in CIE coordinates of (0.152, 0.034) and (0.151, 0.035), respectively. Corresponding small Stokes shifts of 13 and 11 nm were calculated, attributed to the rigidity of the MR framework, which effectively reduced molecular vibrations. These results are consistent with the computational simulations. Furthermore, based on the low-temperature Fl and Phos spectra in toluene, the calculated energy levels for the lowest singlet (S_1) and triplet (T_1) states are 2.88/2.69 eV and 2.87/2.69 eV, yielding similar ΔE_{ST} of 0.19 eV and 0.18 eV for **DBNO** and **DMBNO**, respectively (Fig. S20†). Such small ΔE_{ST} values can facilitate the RISC process under ambient conditions, thereby realizing TADF characteristics.

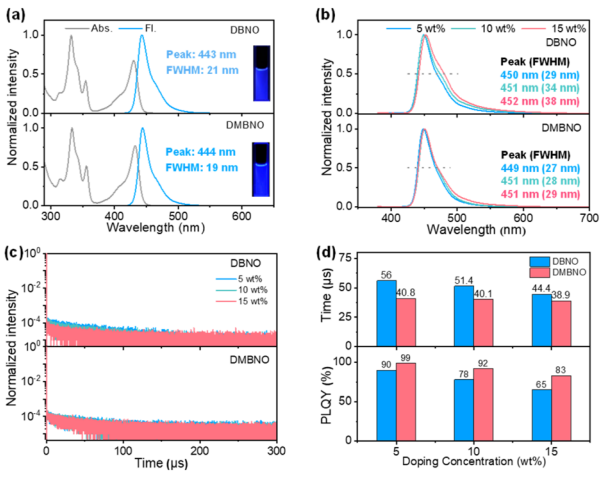

Fig. 4 Photophysical properties of **DBNO** and **DMBNO**. (a) The UV-vis spectra and fluorescence spectra in diluted toluene (inset: photographs of corresponding diluted toluene under 365 nm UV light excitation). (b) The fluorescence spectra in $SiTrzCz_2$ doped films. (c) Transient photoluminescence decay curves in $SiTrzCz_2$ doped films. (d) The delayed fluorescence (τ_D) lifetimes and PLQY values (Φ_{PL}) in $SiTrzCz_2$ doped films.

As with most of the MR-TADF emitters, both emitters display red-shifted and broadened emission in 5 wt% 9,9′-(6-(3-(triphenylsilyl)phenyl)-1,3,5-triazine-2,4-diyl)bis(9*H*-carbazole) ($SiTrzCz_2$) films, with peak/FWHM values of 450/29 nm and 449/27 nm, respectively. Of note, the FWHM of **DBNO** increases significantly as the doping concentration is raised from 5 wt% to 15 wt% (Fig. 4b), while **DMBNO** exhibits only slight broadening, indicating better resistance to spectral broadening. Both emitters demonstrate high PLQYs above 90% in 5 wt% doped films. However, for **DBNO**, PLQYs drop sharply to 78% and 65% at doping concentrations of 10 wt% and 15 wt%, respectively (Fig. 4d). In contrast, **DMBNO** shows a smaller decline in PLQY with increasing concentration, suggesting superior anti-quenching properties, which may deliver superior performance at high doping concentrations. To further understand the dipole orientations of these emitters, angle-resolved PL measurements were performed on doped films. Both emitters demonstrate remarkably high $\theta_{\parallel}$ values exceeding 90% (Fig. S22†), which can significantly enhance the EQE of OLEDs by improving out-coupling efficiency (η_{out}).

The TADF properties of **DBNO** and **DMBNO** were subsequently evidenced by transient photoluminescence (PL) spectra recorded on doped films. As depicted in Fig. 4c, both emitters exhibit distinct bi-exponential decay patterns, with fitted prompt/delayed (τ_{PF}/τ_{DF}) lifetimes of 4.5 ns/56.0 μs for **DBNO** and 3.4 ns/40.8 μs for **DMBNO** in 5 wt% doped films. Key rate constants, including singlet radiative decay ($k_{r,S}$) and RISC (k_{RISC}) were calculated from the transient PL spectra and PLQYs (Tables 1 and S4†). Both emitters exhibit fast $k_{r,S}$ values in the order of 10^8 s^{-1} and moderate k_{RISC} values in the order of 10^4 s^{-1}, consistent with typical MR-TADF materials. The temperature-dependent transient PL decay curves further substantiated the TADF characteristics of the emitters, with the intensity of the delayed fluorescence component progressively enhancing as the temperature increased (Fig. S23†). Notably, both delayed lifetimes and delayed proportions of **DBNO** decrease significantly with increasing doping concentration from 5 wt% to 15 wt%. In contrast, this decline is very small for **DMBNO**, further indicating that **DMBNO** will have better EL performance at high doping concentrations.

Electroluminescent properties

To assess the electroluminescent (EL) performance of **DBNO** and **DMBNO**, OLED were fabricated with the following architecture: indium tin oxide (ITO)/dipyrazino[2,3-*f*:2′,3′-*h*] quinoxaline-2,3,6,7,10,11-hexacarbonitrile (HATCN, 5 nm)/1,1-bis((di-4-tolylamino)phenyl)-cyclohexane (TAPC, 30 nm)/4,4′,4″-tris(*N*-carbazolyl)-triphenylamine (TCTA, 15 nm)/1,3-di(9*H*-carbazol-9-yl)benzene (mCBP, 20 nm)/EML, 25 nm/9,9′-(6-(3-(triphenylsilyl)phenyl)-1,3,5-triazine-2,4-diyl)bis(9*H*-carbazole) ($SiTrzCz_2$, 10 nm)/1-(4-(10-([1,1′-biphenyl]-4-yl)anthracen-9-yl)phenyl)-2-ethyl-1*H*-benzo[*d*]-imidazole (ANT-BIZ, 30 nm)/hydroxyquinolinolato-lithium (Liq, 2 nm)/aluminum (Al, 100 nm). Here, ITO and Al serve as anode and cathode, while HATCN and Liq function as the hole injection layer and electron injection layer, respectively. TAPC and TCTA facilitate hole

Table 1 Photophysical properties of **DBNO** and **DMBNO**

Emitter	λ_{abs}[a] [nm]	λ_{em}[a,b] [nm]	FWHM[a,b] [nm]	ΔE_{ST}[c] [eV]	Φ_{PL}[d] [%]	τ_{PF}[e] [ns]	τ_{DF}[e] [μs]	$k_{r,S}$[f] [10^8 s^{-1}]	$k_{nr,S}$[f] [10^6 s^{-1}]	k_{RISC}[f] [10^4 s^{-1}]	$\theta_{\parallel}$[g] [%]
DBNO	430	443/450	21/29	0.19	90	4.5	56.0	1.24	13.8	2.88	93
DMBNO	433	444/449	19/27	0.18	99	3.4	40.8	1.54	1.56	4.62	95

[a] Measured in toluene (1×10^{-5} M). [b] Measured in 5 wt% doped $SiTrzCz_2$ film. [c] $\Delta E_{ST} = S_1 - T_1$. [d] Absolute PL quantum yield evaluated using an integrating sphere under argon atmosphere in 5 wt% doped $SiTrzCz_2$ film. [e] The prompt fluorescence (τ_P) and delayed fluorescence (τ_D) lifetimes in 5 wt% doped $SiTrzCz_2$ film. [f] The radiative, non-radiative rate constants of S_1 to S_0 ($k_{nr,S}$) and the rate constants of reverse intersystem crossing (k_{RISC}). [g] The characterizations of the horizontal dipole orientation ($\theta_{\parallel}$) were obtained from the angle-dependent *p*-polarized PL spectra.

transporting layers, while mCBP and $SiTrzCz_2$ serve as exciton-blocking layers. ANT-BIZ acts as the electron transport layer. In the construction of the emitting layer (EML), $SiTrzCz_2$ was selected as host matrix owing to its compatible HOMO/LUMO energy levels with adjacent emitters and functional layers, appropriate triplet energy level, and substantial emission spectral overlap with the absorption spectra of emitters. The doping concentration of the emitters were set to 5 wt%, 10 wt%, and 15 wt%. The energy level alignment, chemical structures of functional layer materials, and the EL performance are depicted in Fig. 5 and S24–S27,† and the corresponding key parameters are summarized in Table 2.

As shown in Fig. 5 and Table 2, all devices exhibit deep-blue emission peaking within the range of 447–450 nm, with a narrow FWHM as small as 24 nm across doping concentrations ranging from 5 wt% to 15 wt%. Notably, consistent with PL, the emission peak and FWHM of **DMBNO** undergo only slight alterations as the doping concentration increases, compared to **DBNO**. This stability can be ascribed to the incorporation of multi-mesityl groups, which substantially augments the intermolecular stacking distance and efficiently mitigates π–π stacking interactions. Consequently, the augmented inhibition of aggregation establishes a robust basis for sustaining high color purity at elevated doping concentrations. This results in high color purity with CIE_y values around 0.046. For **DBNO**-based devices, the optimal EQE of 27.2% is achieved at a 5 wt% doping concentration. However, increasing the doping concentration to 10 wt% and 15 wt% results in a sharp decline in EQE, primarily due to the severe aggregation-caused quenching (ACQ) effect, consistent with the PLQY results. Interestingly, devices based on **DMBNO** not only exhibit nearly identical EL spectra but also achieve high EQE values exceeding 30%. Unlike **DBNO**, the EQE of **DMBNO**-based OLEDs follows a trend of initially increasing and then decreasing with increasing concentrations. Notably, the 10 wt% **DMBNO**-based device demonstrates an exceptional EQE_{max} of 32.3% without employing any light out-coupling enhancement techniques, while maintaining a pure-blue EL spectrum with a CIE_y value of 0.046, fully satisfying the BT.2020 blue standard. The high efficiency and excellent color purity can be attributed to the TADF properties, distinguished PLQY, high $\theta_{\parallel}$, a suitable emission spectrum, and the ability to suppress quenching and spectral broadening of **DMBNO**. Although all devices experienced fair efficiency roll-off, the high EQE of 32.3% and CIE_y value of 0.046 position **DMBNO** as one of the top-performing emitters for deep-blue MR-TADF OLEDs, validating the effectiveness of our molecular design strategy.

To further enhance device performance and mitigate efficiency roll-off, a TADF-sensitizing approach was employed using **DMBNO**, leveraging its excellent color purity and fast rate of singlet radiative decay. Specifically, 9,9′,9″,9‴,9⁗-(6-(5,9-dioxa-13*b*-boranaphtho[3,2,1-*de*]anthracen-7-yl)benzene-1,2,3,4,5-pentayl)pentakis(3,6-di-*tert*-butyl-9*H*-carbazole) (5TBUCz-BO) was selected as a TADF sensitizer due to its well-matched PL spectrum with the absorption spectrum of **DMBNO** (Fig. S28†). Meanwhile, 2,8-bis(diphenylphosphine oxide)dibenzofuran (PPF) was utilized as the host matrix because of its high triplet energy level and energy matching with the sensitizer. **DMBNO** served as the emitter, with host, sensitizer, and emitter concentrations set to 79 wt%, 20 wt%, and 1 wt%, respectively. As depicted in Fig. 5e, the sensitized device

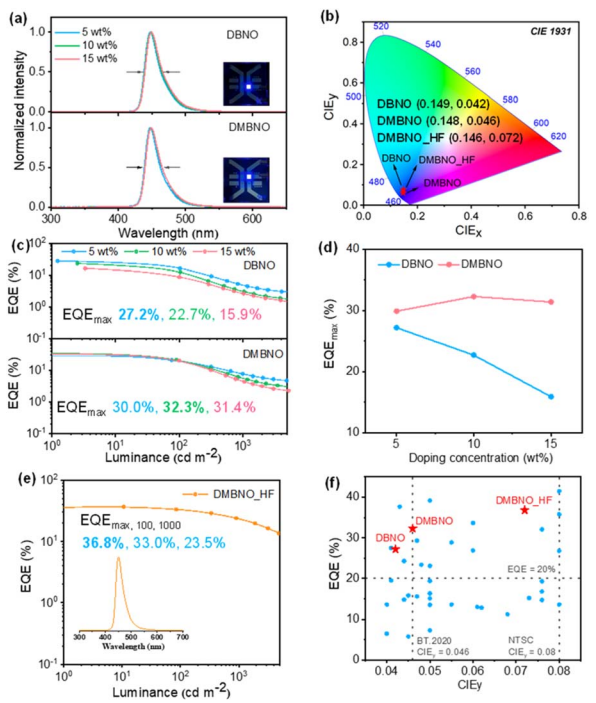

Fig. 5 (a) The EL spectra of the devices (recorded at 6 V). (b) CIE coordinates of EL emission from 5 wt% **DBNO**, 10 wt% **DMBNO** devices and HF-device of **DMBNO**. (c) EQE–luminance (EQE–L) curves of **DBNO** and **DMBNO**. (d) The EQE_{max}–dopant concentration relationships of **DBNO** and **DMBNO**. (e) The EQE–L curve of **DMBNO** based hyperfluorescent device, inset: EL spectrum recorded at 6 V. (f) Summary of the reported MR-TADF emitters with CIE_y less than 0.08.

Table 2 Summary of the EL data

Emitter	Conc. [wt%]	V_{on}[a] [V]	λ_{EL}[b] [nm]	FWHM[b] [nm]	L_{max}[c] [cd m^{-2}]	CE_{max}[d] [cd A^{-1}]	PE_{max}[e] [lm W^{-1}]	EQE[f] [%]	CIE[b] (x, y)
DBNO	5	3.2	447	25	8538	12.6	12.4	27.2/16.2/4.8	0.149, 0.042
	10	3.2	448	26	5935	11.4	11.2	22.7/12.2/3.1	0.148, 0.047
	15	3.2	450	27	5611	8.6	8.4	15.9/8.6/2.6	0.148, 0.052
DMBNO	5	3.6	448	24	12 432	13.8	12.0	30.0/19.2/7.6	0.149, 0.041
	10	3.6	449	25	8727	16.2	14.2	32.3/20.7/5.5	0.148, 0.046
	15	3.6	449	25	7021	17.0	14.8	31.4/20.2/4.5	0.148, 0.049

[a] Turn-on voltage recorded at the luminance of 1 cd m^{-2}. [b] Recorded at 6 V. [c] Maximum brightness. [d] Maximum current efficiency. [e] Maximum power efficiency. [f] EQE at maximum, 100, and 1000 cd m^{-2}.

maintains deep-blue emission with CIE coordinates of (0.146, 0.072). More importantly, the device achieves an ultra-high EQE_{max} of 36.8% with reduced efficiency roll-off at high brightness: EQE values of 33.0% at 100 cd m^{-2} and 23.5% at 1000 cd m^{-2}, representing EQE drops of only 10% and 36%, respectively. The enhanced EQE and the improved efficiency roll-off can be attributed to the efficient energy transfer from the sensitizer to the emitter, facilitated by Förster resonance energy transfer (FRET) (Fig. S30†), as well as the rapid exciton dynamic process resulting from the combination of the sensitizer's fast up-conversion process and the fast radiative process of **DMBNO**, which mitigates the quenching of triplet excitons at high luminance, increasing the exciton utilization rate. As illustrated in Fig. 5f, **DMBNO** stands out among the most efficient reported deep-blue MR-TADF emitters, excelling in both CIE_y and EQE_{max}, further underscoring its remarkable performance.

Conclusions

In summary, we have developed a straightforward yet effective molecular design strategy to achieve highly efficient deep-blue MR-TADF emitters by incorporating a double B–N–O embedded MR skeleton with peripheral multi-mesityl group decorations. The resulting emitters demonstrated deep-blue narrowband emission with near-unity PLQYs and ideal $\theta_{\|}$ values in solid states. Notably, the proof-of-concept molecule of **DMBNO** exhibited quenching resistance and suppression of spectral broadening in solid states. Consequently, OLEDs based on **DMBNO** displayed virtually identical EL spectra and achieved impressive EQEs exceeding 30% across a wide doping concentration range from 5 wt% to 15 wt%. In particular, the 10 wt% **DMBNO**-based device achieved a remarkable EQE of 32.3%, with a CIE_y value of 0.046, fully meeting the BT.2020 blue gamut. Additionally, through the incorporation of a TADF-sensitizing approach, the EQE was further enhanced to 36.8%. We believe that the findings provide valuable guidance for the development of high-performance narrowband emitters possessing anti-quenching characteristics.

Data availability

All data supporting the findings of this study are presented in the article and ESI.† Additional data are available from the corresponding author upon reasonable request.

Author contributions

Z. Huang and C. Yang supervised the project. Z. Xue synthesized and characterized the chemical and optoelectronic properties of the compounds. Z. Xue and Z. Huang wrote the manuscript. Z. Xiao and Y. Zou provided the sensitizer. Z. Chen performed a part of the quantum chemical calculations. J. Liu contributed to the angle-resolved PL measurements. All authors contributed to the discussion of the results.

Conflicts of interest

There are no conflicts to declare.

Acknowledgements

This work was supported by National Natural Science Foundation of China (No. 52130308 and 21805195), the Guangdong Basic and Applied Basic Research Foundation (2023A1515030005), the Shenzhen Science and Technology Innovation Commission (JCYJ20220531101215034 and ZDSYS20210623091813040), and the Research Team Cultivation Program of Shenzhen University (2023DFT004). We thank the Instrumental Analysis Center of Shenzhen University for analytical support.

References

1 G. Hong, X. Gan, C. Leonhardt, Z. Zhang, J. Seibert, J. M. Busch and S. Bräse, *Adv. Mater.*, 2021, **33**, 2005630.
2 R. M. Soneira, *J. Soc. Inf. Disp.*, 2016, **32**, 26–31.
3 H.-J. Tan, G.-X. Yang, Y.-L. Deng, C. Cao, J.-H. Tan, Z.-L. Zhu, W.-C. Chen, Y. Xiong, J.-X. Jian, C.-S. Lee and Q.-X. Tong, *Adv. Mater.*, 2022, **34**, 2200537.
4 X. Fan, X. Hao, F. Huang, J. Yu, K. Wang and X. Zhang, *Adv. Sci.*, 2023, **10**, 2303504.
5 H. Uoyama, K. Goushi, K. Shizu, H. Nomura and C. Adachi, *Nature*, 2012, **492**, 234–238.
6 J. Han, Y. Chen, N. Li, Z. Huang and C. Yang, *Aggregate*, 2022, **3**, e182.
7 D. H. Ahn, S. W. Kim, H. Lee, I. J. Ko, D. Karthik, J. Y. Lee and J. H. Kwon, *Nat. Photonics*, 2019, **13**, 540–546.

8 T. Hatakeyama, K. Shiren, K. Nakajima, S. Nomura, S. Nakatsuka, K. Kinoshita, J. Ni, Y. Ono and T. Ikuta, *Adv. Mater.*, 2016, **28**, 2777–2781.
9 I. S. Park, M. Yang, H. Shibata, N. Amanokura and T. Yasuda, *Adv. Mater.*, 2022, **34**, 2107951.
10 J. Park, J. Lim, J. H. Lee, B. Jang, J. H. Han, S. S. Yoon and J. Y. Lee, *ACS Appl. Mater. Interfaces*, 2021, **13**, 45798–45805.
11 Z. Ye, H. Wu, Y. Xu, T. Hua, G. Chen, Z. Chen, X. Yin, M. Huang, K. Xu, X. Song, Z. Huang, X. Lv, J. Miao, X. Cao and C. Yang, *Adv. Mater.*, 2024, **36**, 2308314.
12 R. W. Weerasinghe, S. Madayanad Suresh, D. Hall, T. Matulaitis, A. M. Z. Slawin, S. Warriner, Y.-T. Lee, C.-Y. Chan, Y. Tsuchiya, E. Zysman-Colman and C. Adachi, *Adv. Mater.*, 2024, **36**, 2402289.
13 J. Han, Z. Huang, X. Lv, J. Miao, Y. Qiu, X. Cao and C. Yang, *Adv. Opt. Mater.*, 2022, **10**, 2102092.
14 G. Li, M. Du, T. Fan, X. Luo, L. Duan and Y. Zhang, *Mater. Today*, 2024, **73**, 30–37.
15 H. Jiang, J. Jin and W.-Y. Wong, *Adv. Funct. Mater.*, 2023, **33**, 2306880.
16 Y. Zou, M. Yu, Y. Xu, Z. Xiao, X. Song, Y. Hu, Z. Xu, C. Zhong, J. He, X. Cao, K. Li, J. Miao and C. Yang, *Chem*, 2024, **10**, 1485–1501.
17 X. Cai, Y. Pan, C. Li, L. Li, Y. Pu, Y. Wu and Y. Wang, *Angew. Chem., Int. Ed.*, 2024, **63**, e202408522.
18 X. Huang, J. Liu, Y. Xu, G. Chen, M. Huang, M. Yu, X. Lv, X. Yin, Y. Zou, J. Miao, X. Cao and C. Yang, *Natl. Sci. Rev.*, 2024, **11**, nwae115.
19 Y. Wang, R. Guo, A. Ying, K. Di, L. Chen, H. Gu, S. Liu, Y. Duan, H. Su, S. Gong and L. Wang, *Adv. Opt. Mater.*, 2023, **11**, 2202034.
20 Z. Huang, H. Xie, J. Miao, Y. Wei, Y. Zou, T. Hua, X. Cao and C. Yang, *J. Am. Chem. Soc.*, 2023, **145**, 12550–12560.
21 B. Lei, Z. Huang, S. Li, J. Liu, Z. Bin and J. You, *Angew. Chem., Int. Ed.*, 2023, **62**, e202218405.
22 S. Wang, Y. Xu, J. Miao, T. Hua, X. Cao, N. Li, Z. Huang and C. Yang, *Chem. Eng. J.*, 2023, **471**, 144664.
23 S. Oda, W. Kumano, T. Hama, R. Kawasumi, K. Yoshiura and T. Hatakeyama, *Angew. Chem., Int. Ed.*, 2021, **60**, 2882–2886.
24 S. Oda, B. Kawakami, M. Horiuchi, Y. Yamasaki, R. Kawasumi and T. Hatakeyama, *Adv. Sci.*, 2023, **10**, 2205070.
25 Y. Kondo, K. Yoshiura, S. Kitera, H. Nishi, S. Oda, H. Gotoh, Y. Sasada, M. Yanai and T. Hatakeyama, *Nat. Photonics*, 2019, **13**, 678–682.
26 H. Tanaka, S. Oda, G. Ricci, H. Gotoh, K. Tabata, R. Kawasumi, D. Beljonne, Y. Olivier and T. Hatakeyama, *Angew. Chem., Int. Ed.*, 2021, **60**, 17910–17914.
27 X. Lv, J. Miao, M. Liu, Q. Peng, C. Zhong, Y. Hu, X. Cao, H. Wu, Y. Yang, C. Zhou, J. Ma, Y. Zou and C. Yang, *Angew. Chem., Int. Ed.*, 2022, **61**, e202201588.
28 X. Wang, Y. Zhang, H. Dai, G. Li, M. Liu, G. Meng, X. Zeng, T. Huang, L. Wang, Q. Peng, D. Yang, D. Ma, D. Zhang and L. Duan, *Angew. Chem., Int. Ed.*, 2022, **61**, e202206916.
29 K. R. Naveen, J. H. Oh, H. S. Lee and J. H. Kwon, *Angew. Chem., Int. Ed.*, 2023, **62**, e202306768.
30 J. Ochi, Y. Yamasaki, K. Tanaka, Y. Kondo, K. Isayama, S. Oda, M. Kondo and T. Hatakeyama, *Nat. Commun.*, 2024, **15**, 2361.
31 K. Rayappa Naveen, H. Lee, R. Braveenth, K. Joon Yang, S. Jae Hwang and J. Hyuk Kwon, *Chem. Eng. J.*, 2022, **432**, 134381.
32 T. Hua, X. Cao, J. Miao, X. Yin, Z. Chen, Z. Huang and C. Yang, *Nat. Photonics*, 2024, **18**, 1161–1169.
33 K. Stavrou, A. Danos, T. Hama, T. Hatakeyama and A. Monkman, *ACS Appl. Mater. Interfaces*, 2021, **13**, 8643–8655.
34 K. Matsui, S. Oda, K. Yoshiura, K. Nakajima, N. Yasuda and T. Hatakeyama, *J. Am. Chem. Soc.*, 2018, **140**, 1195–1198.
35 P. Jiang, J. Miao, X. Cao, H. Xia, K. Pan, T. Hua, X. Lv, Z. Huang, Y. Zou and C. Yang, *Adv. Mater.*, 2022, **34**, 2106954.
36 Y.-K. Qu, D.-Y. Zhou, F.-K. Kong, Q. Zheng, X. Tang, Y.-H. Zhu, C.-C. Huang, Z.-Q. Feng, J. Fan, C. Adachi, L.-S. Liao and Z.-Q. Jiang, *Angew. Chem., Int. Ed.*, 2022, **61**, e202201886.
37 X.-F. Luo, H.-X. Ni, X. Liang, D. Yang, D. Ma, Y.-X. Zheng and J.-L. Zuo, *Adv. Opt. Mater.*, 2023, **11**, 2203002.
38 H.-X. Ni, J.-Z. Zhu, J.-J. Hu, L. Yuan, X.-J. Liao, S. Xing and Y.-X. Zheng, *Adv. Opt. Mater.*, 2024, **12**, 2401033.
39 Y. Wang, Z. Ma, J. Pu, D. Guo, G. Li, Z. Chen, S.-J. Su, H. Deng, J. Zhao and Z. Chi, *Aggregate*, 2024, **5**, e585.
40 Y. Zhang, J. Wei, D. Zhang, C. Yin, G. Li, Z. Liu, X. Jia, J. Qiao and L. Duan, *Angew. Chem., Int. Ed.*, 2022, **61**, e202113206.
41 J. Bian, S. Chen, L. Qiu, R. Tian, Y. Man, Y. Wang, S. Chen, J. Zhang, C. Duan, C. Han and H. Xu, *Adv. Mater.*, 2022, **34**, 2110547.
42 H.-J. Cheon, S.-J. Woo, S.-H. Baek, J.-H. Lee and Y.-H. Kim, *Adv. Mater.*, 2022, **34**, 2207416.
43 J. Jin, M. Chen, H. Jiang, B. Zhang, Z. Xie and W.-Y. Wong, *ACS Mater. Lett.*, 2024, **6**, 3246–3253.
44 L. Wu, Z. Huang, J. Miao, S. Wang, X. Li, N. Li, X. Cao and C. Yang, *Angew. Chem., Int. Ed.*, 2024, **63**, e202402020.